



HAL
open science

POD-Galerkin advection model for convective flow Application to a flapping rectangular supersonic jet

V. Jaunet, E Collin, J Delville

► **To cite this version:**

V. Jaunet, E Collin, J Delville. POD-Galerkin advection model for convective flow Application to a flapping rectangular supersonic jet. *Experiments in Fluids*, 2016, 10.1007/s00348-016-2156-2. hal-02339478

HAL Id: hal-02339478

<https://hal.science/hal-02339478>

Submitted on 30 Oct 2019

HAL is a multi-disciplinary open access archive for the deposit and dissemination of scientific research documents, whether they are published or not. The documents may come from teaching and research institutions in France or abroad, or from public or private research centers.

L'archive ouverte pluridisciplinaire **HAL**, est destinée au dépôt et à la diffusion de documents scientifiques de niveau recherche, publiés ou non, émanant des établissements d'enseignement et de recherche français ou étrangers, des laboratoires publics ou privés.

POD-Galerkin advection model for convective flow

Application to a flapping rectangular supersonic jet

V. Jaunet · E. Collin · J. Delville

Received: / Accepted:

Abstract This article describes a model obtained by applying Proper Orthogonal Decomposition to the advection equation. The resulting set of equations links the POD modes, their temporal and spatial derivatives and the flow convection velocity. It provides a technique to calculate the convection velocity of coherent structures. It follows, from the model, that *a priori* knowledge of the convection velocity suffices to construct a dynamical model of the flow. This is demonstrated using experimental data.

Keywords Supersonic jet, Proper Orthogonal Decomposition, Convection velocity, Advection equation, Low order dynamical systems

Nomenclature

$, x$	Space derivative
$, t$	Time derivative
e	External flow
j	Jet flow
$\Phi^{(n)}(\mathbf{x})$	Spatial POD mode of order n
$a^{(n)}(t)$	Temporal POD coefficient of order n
f_s	Screech frequency
$g(\mathbf{x}, t)$	Spatio-temporal field
h_j	Size of the nozzle
L_j	Height of the nozzle
M	Mach number
M_e	External flow Mach number

U_c Convection velocity

1 Introduction

The convection velocity of organized structures is an important feature that, together with a length scale, permits in estimating the main frequency of a phenomenon. For example, it is one of the key parameters used to predict screech tones of high speed jets (Powell, 1953b,a).

In order to estimate this convection velocity many different methods can be employed, all of them requiring time and/or space separation.

Two-point hotwire, LDA or unsteady pressure sensing can be used to discretize the space-time correlation function. The convection speed is obtained as the ratio between the space separation of the two sensors and the lag-time of the maximum correlation value between the two signals (Morris and Zaman, 2010; Kerherve et al., 2004). However, these methods only give access to a local representation of the convection velocity: lots of effort is then required to probe large area of flows.

Particle Image Velocimetry (PIV) gives access to instantaneous velocity fields, it is thus particularly well suited to measure convection velocity. When time-resolved data can be obtained, the former method can still be used and the entire flow field can be probed. However, the sampling rate attainable with PIV is in many cases not yet sufficient to fully resolve the structures of interest. Shih et al. (1995) and Alkisar et al. (2003) defined the convection velocity as the vorticity weighted average value within the area of flow in a coherent structure. A single PIV snapshot suffices to deduce the speed of a structure. The results obtained with this definition may however be sensitive to the way the coherent structures

are defined and identified in the data.

Two-spark schlieren imaging has already been used years ago to obtain the velocity of coherent structures in high-speed mixing layers (Papamoschou, 1989). The identification of coherent structures in the images was left to the subjectivity of the experimentalists.

Therefore, the aim of this paper is to describe a method that gives the speed of coherent structures. This method can be applied to any kind of data (*e.g.* velocity fields, schlieren images...) as long as it is representative of a convective motion. This method is based on the combination of the advection equation and a POD-Galerkin analysis and does not require the data to be time-resolved. As the method used by Papamoschou (1989), two successive samples at short interval time also suffice with this technique. It is therefore particularly well suited to experimental data.

Following the work of Perret et al. (2006), it is shown that the use of this simple model permits the identification of the coefficients of low-order linear dynamical systems, even if the original data only contains independent realizations of a flow field.

The first part of this paper comprises the mathematical description of the POD-Galerkin advection model. In the second part, we describe the experimental set-up and the main flow features. In the third part, the POD-Galerkin model is applied to dual-time Schlieren pictures of a screeching jet to educe the convective speed of large scale structures. Finally, we present the identification of a low order dynamical model, from independent PIV realizations of the same flow field.

2 POD based advection model

2.1 Overview of the Proper Orthogonal Decomposition

We provide here a brief introduction to the Proper Orthogonal Decomposition (POD). The reader can be referred to *e.g.* Sirovich (1987) or Delville (1995) for more precise discussions on POD.

The POD was introduced by Lumley (1967) and consists in considering that the coherent structures are the one having the maximum projection onto the velocity field in a least mean square sense. This leads to an eigenvalue problem whose kernel is the spatial (*classical POD*) or temporal (*Snapshot POD*) correlation tensor. Thus, for a spatio-temporal field $g(\mathbf{x}, t)$ the decomposition is written :

$$g(\mathbf{x}, t) = \sum_{n=1}^{\infty} a^{(n)}(t)\Phi^{(n)}(\mathbf{x}), \quad (1)$$

where $\Phi^{(n)}(\mathbf{x})$ represents the n^{th} eigenfunction (also referred to as spatial mode) and $a^{(n)}(t)$ the n^{th} eigenvector (also referred to as temporal coefficient).

If the database is constituted of uncorrelated samples, the POD decomposition is calculated using the *Snapshot POD* (Sirovich, 1987). The *Snapshot POD* eigenvalue problem is defined as:

$$\int_T C(t, t')a(t')dt' = \lambda a(t), \quad (2)$$

where λ represents the eigenvalue, T the temporal length of the data base, and $C(t, t')$ the temporal correlation matrix calculated on a given spatial domain Ω as:

$$C(t, t') = \frac{1}{T\Omega} \int_{\Omega} g(\mathbf{x}, t)g(\mathbf{x}, t')d\mathbf{x}, \quad (3)$$

The spatial modes are then obtained by projecting the original fields onto the temporal modes :

$$\Phi^{(n)}(\mathbf{x}) = \frac{1}{T\lambda^{(n)}} \int_T g(\mathbf{x}, t)a^{(n)}(t)dt. \quad (4)$$

By definition, the eigenfunction basis $\Phi^{(n)}(\mathbf{x})$ is orthonormal:

$$\langle \Phi^{(n)}(\mathbf{x}), \Phi^{(m)}(\mathbf{x}) \rangle = \delta_{nm}, \quad (5)$$

where $\langle \cdot, \cdot \rangle$ is the scalar product and δ_{nm} is equal to 1 only if $n = m$.

The temporal coefficients $a^{(n)}(t)$ are orthogonal to each other, so that:

$$\langle a^{(n)}a^{(m)} \rangle = \lambda^{(n)}\delta_{nm}, \quad (6)$$

where $\langle \cdot \rangle$ represents the ensemble average.

2.2 Convection velocity estimation

Consider the advection of a fluctuating spatio-temporal field $g(\mathbf{x}, t)$ at velocity U_c :

$$\frac{\partial}{\partial t}g(\mathbf{x}, t) + U_c \frac{\partial}{\partial x}g(\mathbf{x}, t) = 0, \quad (7)$$

The POD decomposition of $g(\mathbf{x}, t)$ is then applied to this equation, leading to:

$$\frac{\partial}{\partial t} \sum_{n=1}^{N_s} a^{(n)}(t)\Phi^{(n)}(\mathbf{x}) + U_c \frac{\partial}{\partial x} \sum_{m=1}^{N_s} a^{(m)}(t)\Phi^{(m)}(\mathbf{x}) = 0. \quad (8)$$

where N_s being the number of available samples (*i.e.* the number of POD modes). This can be written using the linearity of the POD:

$$\sum_{n=1}^{N_s} a_{,t}^{(n)}(t)\Phi^{(n)}(\mathbf{x}) + U_c \sum_{m=1}^{N_s} a^{(m)}(t)\Phi_{,x}^{(m)}(\mathbf{x}) = 0. \quad (9)$$

For reasons of readability, time and space derivatives are referred by the $,t$ and $,x$ underscripts respectively. A Galerkin projection is then performed on a chosen spatial function $\Phi^{(p)}(\mathbf{x})$:

$$\sum_{n=1}^{N_s} a_{,t}^{(n)}(t) \left(\Phi^{(n)}(\mathbf{x}), \Phi^{(p)}(\mathbf{x}) \right) + U_c \sum_{m=1}^{N_s} a^{(m)}(t) \left(\Phi_{,x}^{(m)}(\mathbf{x}), \Phi^{(p)}(\mathbf{x}) \right) = 0. \quad (10)$$

As the eigenfunctions Φ are orthonormal, we get:

$$a_{,t}^{(p)}(t) + U_c \sum_{m=1}^{N_s} a^{(m)}(t) \left(\Phi_{,x}^{(m)}(\mathbf{x}), \Phi^{(p)}(\mathbf{x}) \right) = 0, \quad (11)$$

The last step is to multiply this equation by $a^{(n)}$ and take its ensemble average $\langle \cdot \rangle$:

$$\left\langle a^{(n)} a_{,t}^{(p)} \right\rangle + U_c \lambda^{(n)} \left(\Phi_{,x}^{(n)}(\mathbf{x}), \Phi^{(p)}(\mathbf{x}) \right) = 0. \quad (12)$$

This equation states that, in the case of purely advective flow, there should be a correlation between the scalar product of the spatial POD modes and their space derivatives $\left(\Phi_{,x}^{(n)}(\mathbf{x}), \Phi^{(p)}(\mathbf{x}) \right)$ on one hand, and the correlation weighted by the energy of the temporal POD modes and their temporal derivatives $\left\langle a^{(n)} a_{,t}^{(p)} \right\rangle / \lambda^{(n)}$ on the other. The ratio between the two terms is the convective velocity :

$$U_c = \frac{\lambda^{(n)} \left(\Phi_{,x}^{(n)}(\mathbf{x}), \Phi^{(p)}(\mathbf{x}) \right)}{\left\langle a^{(n)} a_{,t}^{(p)} \right\rangle} \quad (13)$$

Note that in the specific case of $n = p$, the first term of equation 12 becomes:

$$\left\langle a^{(n)} a_{,t}^{(n)} \right\rangle = \frac{1}{2} \frac{\partial}{\partial t} \left\langle (a^{(n)})^2 \right\rangle = \frac{1}{2} \frac{\partial \lambda^{(n)}}{\partial t} = 0, \quad (14)$$

Assuming that the convective velocity is not zero, this means that, in a purely advective flow, the spatial POD modes are orthogonal to their space derivatives:

$$\left(\Phi_{,x}^{(n)}(\mathbf{x}), \Phi^{(n)}(\mathbf{x}) \right) = 0, \quad (15)$$

In other words, a scalar product $\left(\Phi_{,x}^{(n)}(\mathbf{x}), \Phi^{(n)}(\mathbf{x}) \right)$ differing from zero would indicate that the n^{th} mode is not representative of convective motion. This can therefore be used as a criterion to verify if a a POD mode can be used in the POD-Galerkin advection model.

2.3 Dynamical system identification

We would like to emphasize one asset of the former calculations. Consider the system of N_s equations of a linear dynamical system formed with the temporal POD modes:

$$a_{,t}^{(i)} = L_{ij} a^{(j)} + D_i, \quad (16)$$

where L_{ij} is the linear coefficients of the system and D_i constants that represent linear trends. Neglecting the D_i terms, which can almost always be done for stationary signals, multiplying equation 16 by $a^{(j)}$ and taking its ensemble average, we can write:

$$\begin{aligned} \left\langle a_{,t}^{(i)} a^{(j)} \right\rangle &= L_{ij} \left\langle a^{(i)} a^{(j)} \right\rangle \\ \left\langle a_{,t}^{(i)} a^{(j)} \right\rangle &= L_{ij} \lambda^{(j)}, \end{aligned} \quad (17)$$

Hence, the L_{ij} coefficients of the linear dynamical system can be obtained from the temporal POD modes and their time derivatives. This implies time information being obtained (see Perret et al. (2006)), which is not always feasible specially with experimental data.

In the specific case of a known convection velocity, the POD-Galerkin advection model 12 allows us to rewrite the equation 17:

$$U_c \left(\Phi_{,x}^{(i)}(\mathbf{x}), \Phi^{(j)}(\mathbf{x}) \right) = -L_{ij}, \quad (18)$$

showing that in the case of an advective motion of known convective speed, the coefficients of a linear dynamical system of POD modes can be retrieved without the need for temporal information about the flow. Thus, independent realizations of the flow suffice to obtain spatial POD modes, their space derivatives and thus to identify a linear dynamical system.

We have shown that the POD-Galerkin advection model (equation 12) can be used in two different ways:

- Retrieve linear coefficients of a dynamical system, from independent realizations of a purely convective flow (equation 18)
- Obtain the convection velocity, from data containing temporal information (equation 13)

In the following we demonstrate the use of this model onto experimental data obtained from a supersonic rectangular jet.

3 Experimental set-up and flow description

3.1 Wind tunnel

Experiments were conducted in the S150 wind-tunnel of the PPRIME Institute of Poitiers. They consisted of a

Mach number $M = 1.45$ supersonic rectangular supersonic jet of size $h_j = 30$ mm by $L_j = 150$ mm. The geometry of the convergent-divergent nozzle is modified by the addition of two divergents, initially designed in order to study fluidic thrust vectoring (Jaunet et al., 2010). These supplementary divergents consist in 10° slopes of the wall with respect to the main flow direction, on the small sides of the rectangular nozzle. Their length is equal to h_j . As the air flows at supersonic speed, an expansion fan is generated on the corner. Therefore, the pressure of the flow at the exit section of the nozzle is not uniformly distributed and the fully adapted regime can never be reached. The stagnation pressure is set as the minimum pressure necessary to ensure full flowing conditions. It was checked, with oil flow visualizations, that the flow does not separate from the wall before the exit section.

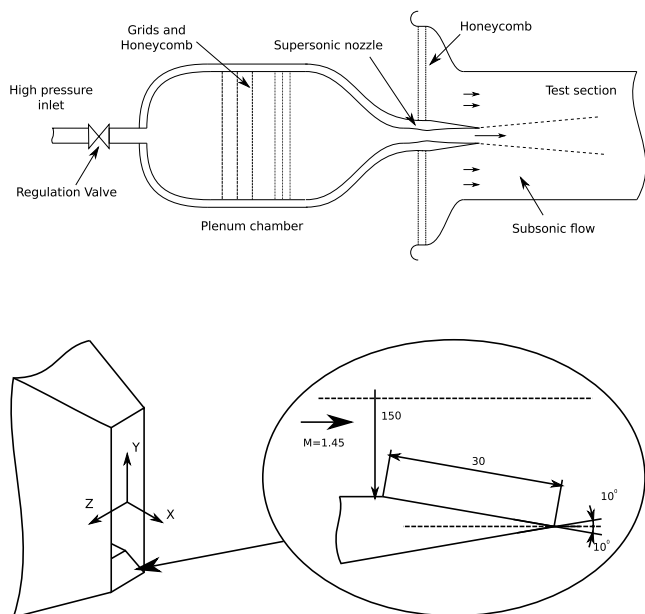


Fig. 1 Schematic diagrams of the wind tunnel (top) and detail of the supersonic nozzle (bottom).

The jet flows into a 500mm square test section. The subsonic surrounding flow, obtained by entrainment of ambient air, flows at a Mach number $M_e = 0.2$.

A reference coordinate system is chosen so that x axis is aligned with the main flow stream and the y axis is parallel to the long sides of the nozzle. The origin of the coordinate system is located in the center of the nozzle exit section (see figure 1).

A sketch of the wind-tunnel together with a detailed view of the nozzle is given in figure 1, and the stagnation conditions and main characteristics of the flow are summarized in table 1.

Table 1 Characteristics of the flow.

	Supersonic jet	Surrounding flow
Dimensions (mm)	150×30	500×500
Mach number	1.45	0.2
Fully expanded Mach number	1.52	-
Velocity (m/s)	380	60
Total pressure (10^5 Pa)	3.7	1
Total temperature (K)	260	290

3.2 Measurements and Visualizations

3.2.1 Unsteady pressure measurements

Two walls of the test section are equipped with KuliteTM sensors, placed on the $y = 0$ plane at a streamwise distance of $x = 8 \times h$. A sketch of the sensor locations with respect to the flow is given in figure 2.

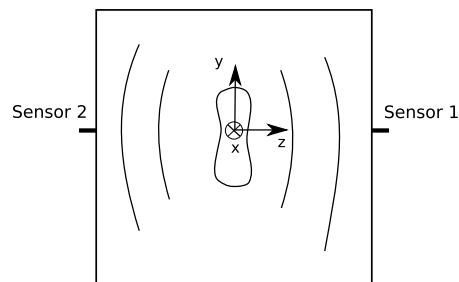


Fig. 2 Schematic diagram of the location of the pressure sensors

The pressure signals were acquired simultaneously at a sample rate of 80kHz after being low pass filtered with a cut-off frequency of 40kHz to avoid any aliasing, and consisted of 2×10^6 samples each, acquired in a single experimental run. In the following, when pressure data is invoked the subscript i refers to the signal of sensor number i . Then, S_{ii} refers to the auto-spectrum of signal i .

3.2.2 Dual-spark schlieren photographs

Pairs of instantaneous schlieren visualizations are acquired using a double spark light source together with a PIV camera. apparatus. The light source comprises a HSPSTM twin nano flash and two spark lamps. Hence, pairs of schlieren visualizations can be performed with a time delay between successive images that can be adjusted up to a minimum of $\Delta t = 1\mu\text{s}$. The 12 bit CCD sensor of the camera is composed of 1200×1600 pixels covering a field of view of about $200\text{mm} \times 200\text{mm}$, so that the resolution is sufficient to study the large scale coherent features of the flow. Synchronization between

the light source and the camera is controlled by a computer.

The two successive sparks of the light source are obtained with two different pairs of electrodes. Consequently, the two successive images may not possess the same exposure and/or contrast and to avoid problems during the post-processing, the energy of each image is normalized and a histogram specification is applied. Histogram specification is performed using the histogram of the average image as a target. Figure 3 presents the histograms of 5 schlieren pictures taken from the data base before and after application of the histogram specification. As can be seen, the post-processed images have now the same exposure, ensuring that future analysis will less be corrupted by illumination fluctuations.

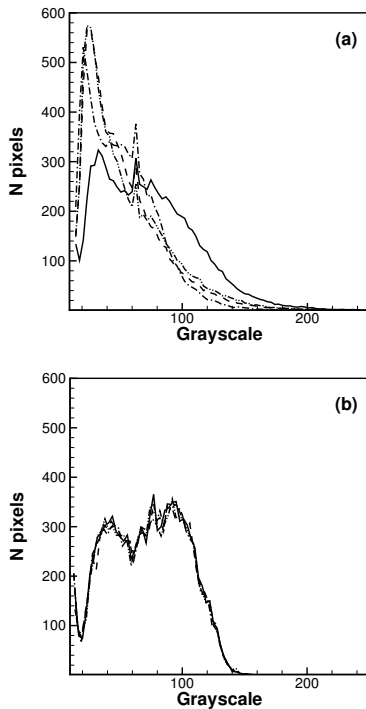


Fig. 3 Gray-scale histograms of 5 different images before histogram specification (a), and after (b)

Schlieren flow visualizations are performed either with a light source axis parallel to y (side view) or z (top view).

3.2.3 Particle Image Velocimetry

Particle image velocimetry (PIV) is performed in the plane of symmetry of the jet ($z = 0$), as well as in the $z = 0.5h_j$ plane *i.e.* along the lipline. The PIV device consists of a 1600x1200 pixel CCD camera equipped

with a 28 mm lens placed perpendicularly to the measurement plane, giving a field of view of $350 \times 270 \text{mm}^2$. A sketch of the set-up is given in figure 5.

The PIV was calibrated by measuring the aspect ratio of images along the diagonal of the field of view. Care was taken during the alignment of the camera to the laser plane so that the aspect ratio remains constant along the field of view, avoiding parallax effects. The lens aperture was set at $f\#4$ to ensure a correct sharpness of the particle image across the entire field of view and that sufficient light reached the camera's sensor. The optical set-up gives a diffraction-limited particle image size of $5.3 \mu\text{m}$ (Adrian, 1991) slightly smaller than the camera pixel size (*i.e.* $7.4 \mu\text{m}$). Since a 190 mJ Nd-YAG laser was used to illuminate the particles, sufficient energy was provided for the particle image to be larger than a pixel size, avoiding pixel-locking. This is illustrated in figure 4 where a typical velocity histogram of a PIV snapshot is plotted. The absence of discrete peaks, expected around the equivalent velocity given by a single pixel displacement ($\simeq 30 \text{m/s}$), shows that no sign of peak-locking is visible in the data.

The flow is seeded with SiO_2 particles. The particle

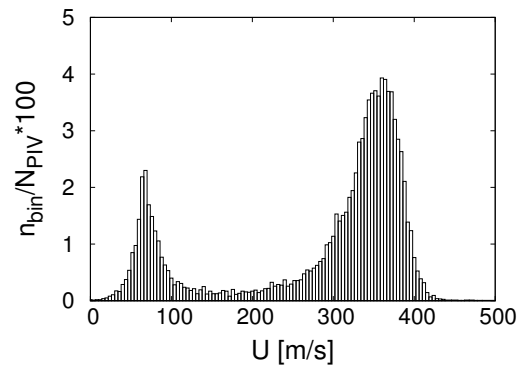


Fig. 4 Velocity histogram of a typical PIV snapshot. The bin width represents 4 m/s.

mean diameter was estimated to $0.3 \mu\text{m}$ and their relaxation time was measured to 0.019ms (Lammari, 1996). This gives an equivalent frequency response of more than 50kHz , which is sufficient for the time scales of interest in this study.

The time separation between each laser illumination for a given particle image pair is set to $7 \mu\text{s}$, which corresponds to a maximum particle displacement of 7 pixels, and a set of 200 pairs of images were acquired at each measurement position. The PIV images are processed using a multi-pass iterative correlation technique (Willert and Gharib, 1991; Soria, 1996) with image deformation to account for local velocity gradients (Scarano, 2002). The process started with interrogation

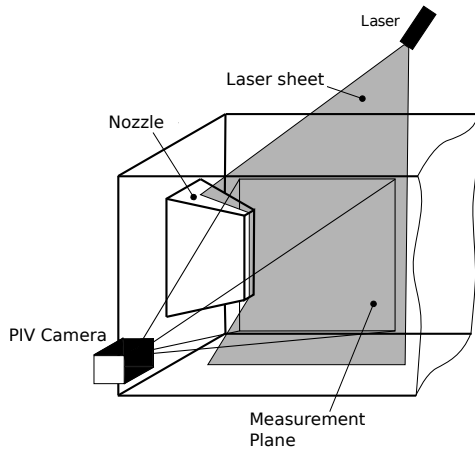


Fig. 5 Schematic diagram of the PIV acquisition system

windows of 64×64 pixels and finished with interrogation areas of 16×16 . The overlap between two successive interrogation areas was set at 50%. At each pass, a peak-ratio validation criterion was used; vectors were rejected if the ratio between the first and the second highest correlation peaks was less than 1.2 ensuring the reliability of a given vector. This gives a final PIV resolution of 1 vector every 2.0mm . Finally a spatial UOD filter (Westerweel and Scarano, 2005) together with a temporal statistical 3-sigma filter were employed to detect spurious vectors from the instantaneous PIV fields. Less than 3% of vectors were rejected and the spurious vectors were replaced using an iterative Gappy POD procedure (Murray and Ukeiley, 2007).

A comparison of the PIV results with measurements made with Laser Doppler Anemometry, obtained in a related work (Jaunet, 2010) is presented in figure 6. An excellent agreement is obtained by the two measurement techniques for the mean flow, showing the ability of the PIV to recover the essential features of the flow, such as the complex network of shock waves and expansion waves existing in the jet. The fluctuation intensities obtained with the PIV set-up are slightly underestimated compared to the ones observed with LDA, this is attributed to low-pass filtering effect of interrogation areas. Nonetheless, both techniques agree well on the location of peak of RMS values. The results presented in figure 6 show the excellent reproducibility of the experiment as well as the reliability of the PIV data.

3.3 Main flow features

An example of top-view spark schlieren picture of the jet (optical axis parallel to the long axis of the rectangular nozzle) is given in figure 7. It is clear that the jet

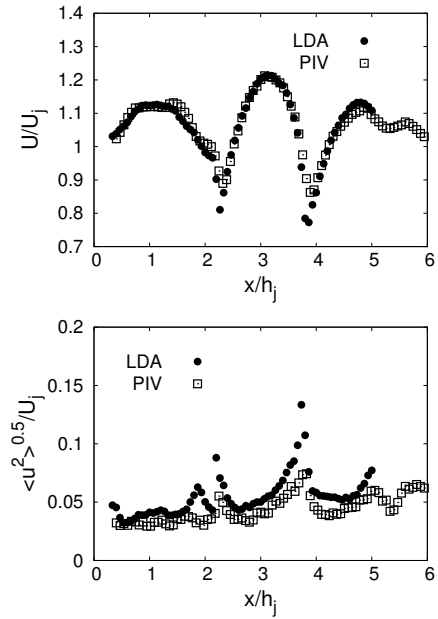


Fig. 6 Comparison of centreline mean (top) and RMS (bottom) velocity profiles obtained with both LDA and PIV.

is undergoing a coherent flapping motion in the (x, z) plane. This motion seems to be coupled with the generation of coherent structures in the mixing layer, in the vicinity of the nozzle lips. These structures are visible on figure 7, they are highlighted by dashed white circles.

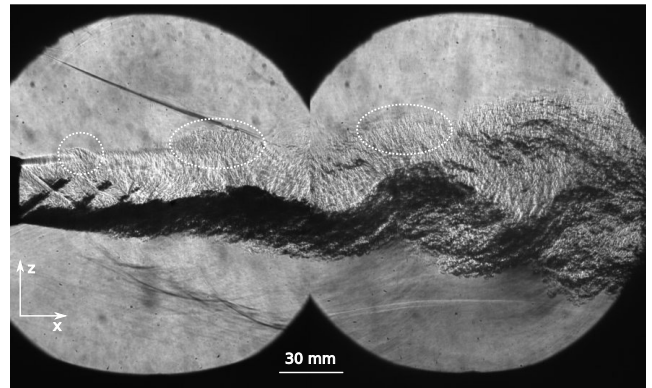


Fig. 7 Spark schlieren picture composed of two chosen independent images, taken from the top view.

This figure also shows that strong acoustic waves exist in the subsonic co-flow. These waves are propagating upstream and are supposed to trigger the creation of the coherent structures when they reach the nozzle lip. This description is very similar to a screech mechanism, but one major difference is the origin and direction of propagation of these acoustic waves. Indeed, in a classical screech phenomenon, the acoustic

perturbations generally emanate spherically from the third or fourth shock cell (Raman, 1999; Alkislar et al., 2003). Here, the acoustic source location could not be seen and seems to be located downstream of the field of view: the waves first reflect on the wall of the wind tunnel before impinging the nozzle lips.

In figure 8 we plot the power spectral density of the pressure signal acquired at the wall of the wind tunnel. Even though the jet does not exhibit a standard screech resonance, the energy of the signal here is also dominated by a fundamental frequency $f_s = 2930\text{Hz}$ and harmonics.

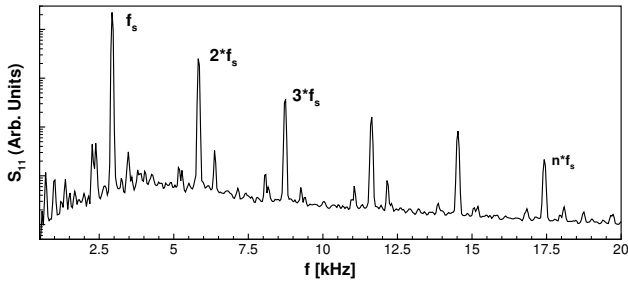


Fig. 8 Power spectral density of wall pressure fluctuations inside the wind tunnel (Sensor 1).

Hence, the main flow features comprise shock cells of various size and a strong flapping of the jet. The mechanism responsible for this very large scale unsteadiness might be found in an acoustic coupling.

4 Application to data from a flapping jet

The results of section 2 are now applied to data obtained from the experiment described previously. First we will show that it is possible to obtain relevant quantitative information (main frequency and convective velocity) on the flow solely based on dual-time schlieren visualization. Then, a low-order linear dynamical system is identified, as presented in section 2, from independent PIV acquisitions allowing us to assess some of the dynamics of the flow field.

4.1 Obtaining a convective velocity

The analysis presented in section 2 is applied in this section to Dual-Spark schlieren photographs. It should be noted that schlieren images contain information integrated along the line of sight. However, the phenomenon of interest in the study is two-dimensional in the (x, z) plane, as it can be seen in the figure 7, so that no direct

bias from the line of sight integration is expected in this part of the study.

4.1.1 Domain of study and POD analysis

As shown in figure 9, the schlieren images show a complex network of discontinuities (*i.e.* shock waves) near the nozzle. This makes a POD analysis difficult in this area: an infinite number of POD modes is necessary to represent the different locations of such discontinuities. Therefore, it has been decided to perform the POD analysis on a sub-domain of the original visualizations, slightly downstream of the nozzle, where no sign of discontinuity is clearly visible. The chosen domain of study, of size $5 \leq x/h \leq 9.5$ and $-1.6 \leq z/h \leq 1.6$, is presented figure 9. This domain was chosen for two reasons. Firstly, it avoids POD analysis on the external flow field, where no feature can be observed, minimizing the computational cost. Secondly, the main objective of the study is to capture the convection speed of the large structures observed in the flow field, so the chosen area includes slightly more than a complete wavelength of the phenomenon, the relevant information of the flapping motion.

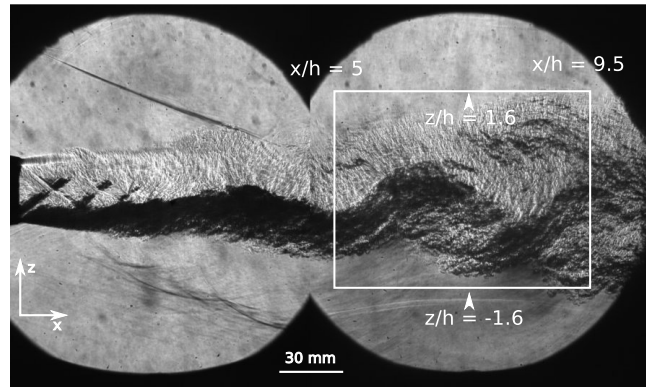


Fig. 9 Definition of the domain of interest on which the POD analysis is performed.

The POD is performed on the fluctuating gray-scale level field $g(\mathbf{x}, t)$ and computed using a *Snapshot POD* (Sirovich, 1987):

$$g(\mathbf{x}, t) = \sum_{n=1}^{N_s} a^{(n)}(t) \Phi^{(n)}(\mathbf{x}), \quad (19)$$

where N_s represents the total number of POD modes given by the number of instantaneous visualizations (200 samples in our case).

As dual-time schlieren photographs were acquired, the time derivative of the temporal coefficients can be calculated with the following scheme:

$$a_{,t}^{(n)}(t + \frac{\Delta t}{2}) = \frac{a^{(n)}(t + \Delta t) - a^{(n)}(t)}{\Delta t}. \quad (20)$$

To preserve the temporal coefficients at the same sampling time than their time derivatives, the temporal modes are interpolated:

$$a^{(n)}(t + \frac{\Delta t}{2}) = \frac{a^{(n)}(t + \Delta t) + a^{(n)}(t)}{2}. \quad (21)$$

Then, the new eigenfunctions are calculated by projecting the gray-scale images onto the interpolated temporal modes using equation 4.

The POD eigenspectrum is plotted in figure 10(a). The energy contained in the first n modes, defined as $\epsilon_n = \sum_{i=1}^n \lambda^i / \sum_{i=1}^{N_s} \lambda^i$, is also plotted in figure 10(b). The first 4 POD modes represent 60% of the total energy and are sufficient to produce partial reconstructions of the flow that well represent the flapping motion of the jet (see figure 11). The higher order POD modes (*i.e.* remaining 40% of the energy) describes the smaller gray-scale wavelength, visible in figure 10(a). These are small turbulent structures, living in the mixing layers, that are also convected downstream. However, the combination of their 3-dimensional motion and the line of sight integration renders the POD analysis unable to correctly capture their convective motion. It is therefore expected that the POD-Galerkin analysis, presented earlier, will only allow us to obtain the convective speed of the large structure of the flapping jet.

The energy of mode 1 and mode 2 on one hand and mode 3 and mode 4 on the other hand are of the same order of magnitude. This results from the fact that the visualizations capture the convective motion of the flow. Indeed, the reproduction of a propagating flow pattern

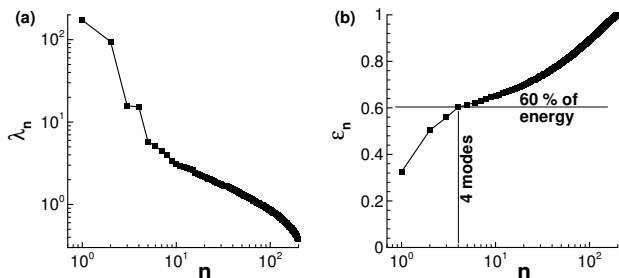


Fig. 10 (a) POD eigenspectrum, (b) partial amount of energy contained in the first n modes ϵ_n .

from eigenfunctions that are fixed in space needs pairs

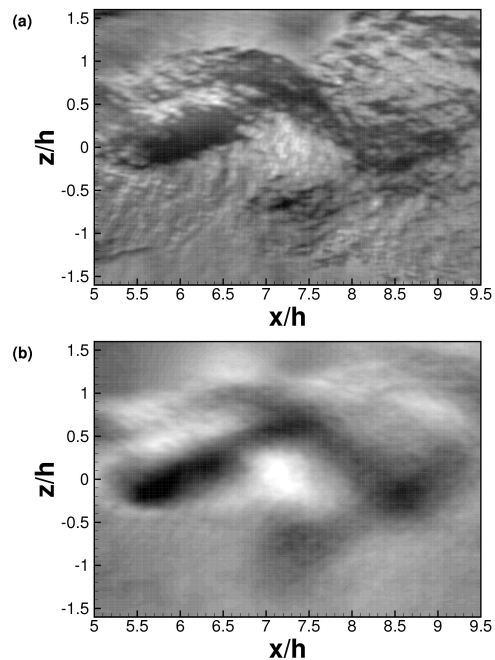


Fig. 11 Comparison of original image (a) and its 4 modes partial reconstruction (b).

of eigenfunctions $\Phi^{(n)}(\mathbf{x})$. Therefore, the temporal dynamics of mode 1 and 2 are very similar, the main difference being a simple phase shift of $\pi/2$. This leads to a simple dynamics in the phase space ($a^{(1)} - a^{(2)}$) in which the temporal modes describe a circle (see figure 12(a)).

The dynamics of mode 3 (and mode 4, not presented here) is the same as the one of mode 1 and mode 2, but occurs at twice the pulsation. This is shown in figure 12. Modes 3 and 4 thus represent the first harmonic of the jet motion.

As can be observed in figure 12, the measured phases do not lie on a perfect circle and some scatter is visible. Some of the time derivatives of the temporal modes, represented as arrows in figure 12, also indicate slightly different directions than the average modes in the phase domain. This can arise for several reasons, either from the jet dynamics itself (screeching jets are well known for staging for example Raman (1999)), or from the schlieren image quality that is sometimes corrupted by slight changes in the illumination quality. Even though a lot of care was taken to account for illumination quality by processing the images, we assume the latter to be responsible for the scatter visible in figure 12. Nevertheless, the method described in the former section uses statistics : the convective velocity is obtained as the ratio of spatial mode scalar products over temporal mode averages (see equation 13), so that uncorrelated

noise should not disturb the estimation of the convection velocity.

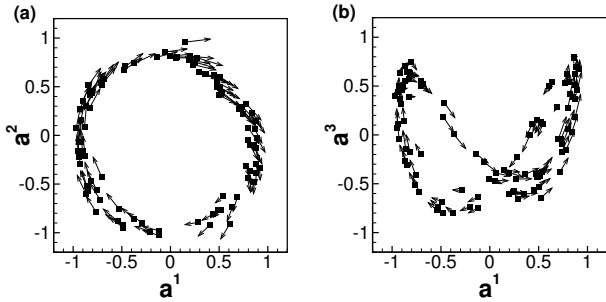


Fig. 12 Phase portraits of the 3 first modes. The arrows represent the time derivatives of the modes.

4.1.2 Flapping frequency estimation

Perret et al. (2006) succeeded in obtaining the main frequency of the flapping motion of a jet-mixing layer interaction using POD analysis and low-order dynamical system. In a very simple way, it is possible to consider a linear low-order dynamical subsystem composed of mode 1 and mode 2, that can be written as follows:

$$a_{,t}^{(i)} = L_{ij}a^{(j)} + D_i, \quad (22)$$

where the subscript $,t$ refers to the time derivative, with implicit summation notation. As the temporal coefficients and their time derivatives are zero-centered, the D_i term can be neglected. Furthermore, in case of a strong correlation between the time derivatives $a_{,t}^{(i)}$ and the coefficients $a^{(j)}$, the dynamical system (22) can be reduced to:

$$\begin{cases} a_{,t}^{(1)}(t) = L_{12} a^{(2)} \\ a_{,t}^{(2)}(t) = L_{21} a^{(1)}, \end{cases} \quad (23)$$

that can easily be integrated giving:

$$\begin{cases} a^{(1)}(t) = K_1 \cos(\omega t + \phi_1) \\ a^{(2)}(t) = K_2 \cos(\omega t + \phi_2), \end{cases} \quad (24)$$

with $\omega = \sqrt{-L_{12}L_{21}} = 2\pi f$. Thus, the characteristic frequency of the flow is directly related to L_{12} and L_{21} .

The phase portraits of $a_{,t}^{(1)}$ versus $a^{(2)}$, and $a_{,t}^{(2)}$ versus $a^{(1)}$ are presented in figure 13. A clear correlation between $a_{,t}^{(1)}$ and $a^{(2)}$ on the one hand, and between $a_{,t}^{(2)}$ and $a^{(1)}$ on the other hand can be observed. A slight scatter of the data can be observed in this figure. This is an effect of the noise observed earlier in figure 12.

Since modes 1 and 2 are of the same order of magnitude, the simple linear dynamical system composed of

these two modes (equation 23) can be used to model the main flow dynamics. A linear regression on the phase portraits leads to $L_{12} = 1.88 \times 10^4 s^{-1} \pm 1.80\%$ and $L_{21} = -1.89 \times 10^4 s^{-1} \pm 1.35\%$. We see that L_{12} and L_{21} have very close values with a small confidence interval, which shows that the noise transmitted from the original data have only a small influence on the results. This gives a flapping frequency $f = 3000 Hz$ obtained with an accuracy of $\pm 1.575\%$.

Hence, the observed flapping motion is periodic with a

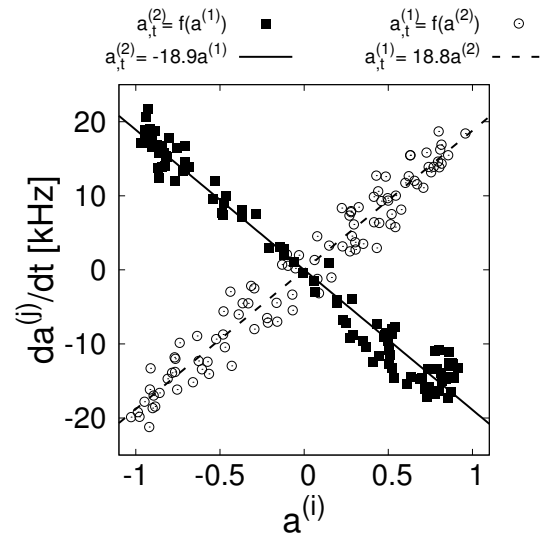


Fig. 13 Frequency estimation of the motion of the 2 first modes

dominant frequency corresponding to the narrow band acoustic waves propagating in the co-flow. This ensures that POD captures the main dynamics of the flow, and it also shows the relevance of performing the analysis downstream of the nozzle.

4.1.3 Convection velocity of large scale structures

In figure 14 are plotted the distributions of $\langle a^{(n)} a_{,t}^{(p)} \rangle / \lambda^{(n)}$ and $(\Phi_{,x}^{(n)}(\mathbf{x}), \Phi^{(p)}(\mathbf{x}))$ in the $(n-p)$ plane for the first 8 modes. Both distributions show a very similar shape which is, as expected from equation 12, signature of the convective feature of the flow. Moreover, one can see that for $n = p$ both the correlation and the scalar product have low values as expected for purely advective flows.

The main differences between these distributions occur for the larger mode numbers. As mentioned earlier, this may be attributed to the fact that the information is integrated along the optical path, the three-dimensionality of the flow at small scales disrupts the

analysis. Moreover, only a small number of samples (100 $(a^{(n)}, a_t^{(p)})$ couples) were used to calculate the POD decomposition, thus higher order modes may have not fully converged.

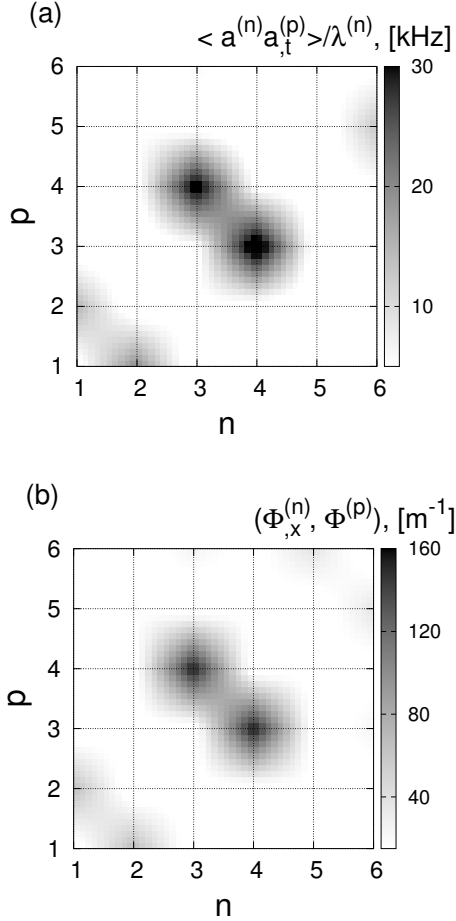


Fig. 14 Comparison of correlations $\langle a^{(n)} a_t^{(p)} \rangle / \lambda^{(n)}$ (a) and scalar products $(\Phi_{,x}^{(n)}(\mathbf{x}), \Phi^{(p)}(\mathbf{x}))$ (b). Values out of the grid points are interpolated.

Nevertheless, a convection speed of the coherent structures of the flow can be obtained using only the first 4 modes. Weighted $\langle a^{(n)} a_t^{(p)} \rangle$ correlations are plotted versus $(\Phi_{,x}^{(n)}(\mathbf{x}), \Phi^{(p)}(\mathbf{x}))$ for $(n, p) \in [1, 4]$ in figure 15. It is possible to see that the points corresponding to the maximum values in the distributions (figure 14) are disposed along a line and, by linear regression, a convective speed of 222.7 m/s is retrieved $\pm 5.16\%$. We see here that the estimation of the convective velocity is more prone to uncertainty than the frequency estimation. This is attributed to the low number of snapshot used for this study. It is likely that the spatial modes and their gradient have perfectly converged. Neverthe-

less, it is a satisfactory result, noting that this analysis is performed on flow visualization.

The estimated convective velocity represents $0.64 \times \Delta U_j$, where ΔU_j is the velocity difference between the jet exit and the entrained subsonic flow. This result is in good agreement with the measured value of Alkislar et al. (2003) and Berland et al. (2007).

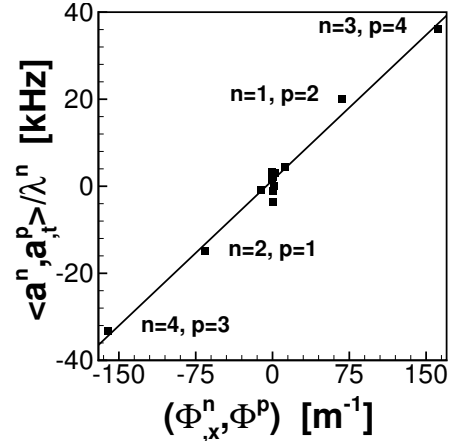


Fig. 15 Estimation of convective velocity of the coherent structures

4.2 Identification of linear dynamical system

As mentioned in 2, equation 12 can be used to identify the coefficients of a linear dynamical system without time-resolved information on the flow. We want to demonstrate a use of the model by applying equation 12 to PIV data from the same flow.

4.2.1 Domain of study and POD analysis

The PIV data is decomposed using POD so that the data can be written as :

$$\mathbf{u}(\mathbf{x}, t) = \sum_{n=1}^{N_s} \alpha^{(n)}(t) \Phi^{(n)}(\mathbf{x}), \quad (25)$$

where \mathbf{u} is the velocity vector. Since the results of 2D PIV contains vertical and horizontal velocity components, the POD spatial modes are now vectors. The POD is performed on a sub-region of the PIV measurement plane, as presented in figure 16. This region is chosen because this is where the jet flapping amplitude is best captured by the PIV. As can be seen on the same figure, the shock waves are weaker in this area, making it easier for the POD to capture the flapping motion of the jet. This region is slightly different than

the area used for the previous analysis, but they overlap in the range $5.0 < x/h_j < 7.6$. Assuming the convection velocity to be a global scale of the jet flow, which is reasonable for the large scales of interest here, it should not be an issue to perform this analysis on two different, but close, regions of the jet.

The cumulative energy of the computed POD modes

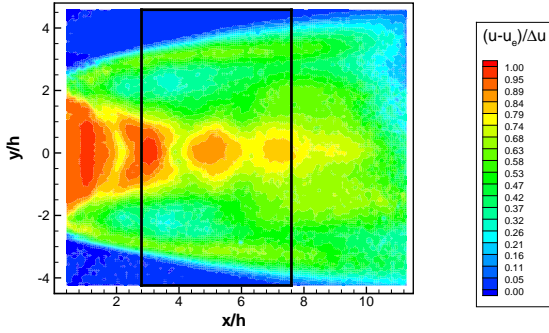


Fig. 16 Mean longitudinal velocity in the $z = 0.5h_j$ plane. The sub-region used for the POD analysis is represented by the black rectangle.

is presented in figure 17(bottom). As can be seen the 5 first POD modes represent only 19% of the total energy of the signal. This low convergence, and the fact that only two distinct modes arise from the POD spectrum (see figure 17(top)) clearly shows that, contrary to the schlieren data set, the PIV data contains more information than the simple flapping motion of the jet. Hence, in this case, the application of the POD-Galerkin model is most likely to be limited to a small number of POD modes, which is acceptable in the sense that only the main flapping motion is of interest here.

The domination of the first POD modes is thus less clear than for the schlieren images (figure 10(b)), but still the 2 first POD modes have an energy of an order of magnitude greater than the higher order modes (see figure 17(top)). Additionally, mode 1 and 2 almost have the same amplitude, which is attributed to the fact that they are representative of a convective motion.

The spatial POD modes $\Phi^{(1)}(\mathbf{x})$ and $\Phi^{(2)}(\mathbf{x})$ are presented in figure 18. It is obvious from this figure that the POD modes mainly contain fluctuations of velocity of a single wavelength. It can also be seen in figure 18 that $\Phi^{(1)}(\mathbf{x})$ and $\Phi^{(2)}(\mathbf{x})$ are in phase quadrature, which is expected if the linear combination of $\Phi^{(1)}(\mathbf{x})$ and $\Phi^{(2)}(\mathbf{x})$ is meant to reproduce a propagating pattern. The phase portrait $\alpha^{(2)}(t) = f(\alpha^{(1)}(t))$ is presented in figure 20. As also observed in the analysis of Edgington-Mitchell et al. (2014), the data is slightly scattered, which is expected giving the slow convergence of the POD spectrum (see figure 17), but

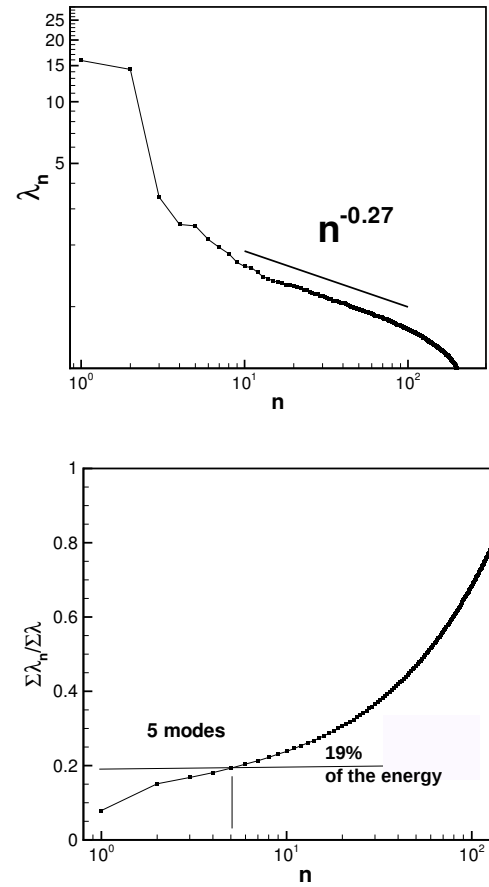


Fig. 17 POD spectrum (top), cumulative energy of the POD modes obtained from the PIV data (bottom)

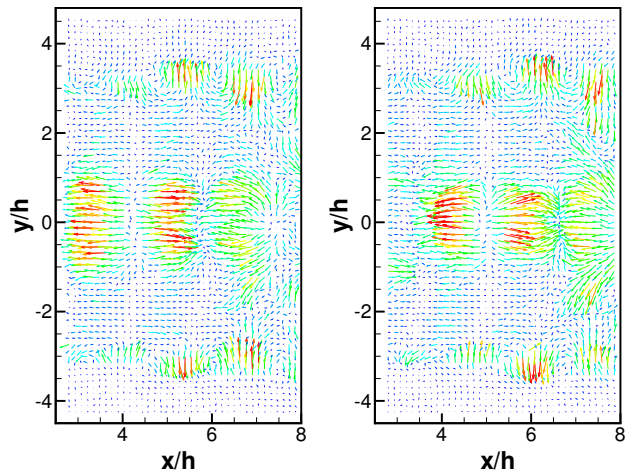


Fig. 18 Two first POD spatial modes $\Phi^{(1)}(\mathbf{x})$ and $\Phi^{(2)}(\mathbf{x})$, left and right respectively. For sake of clarity, colors represent the vector length

is mainly organized in a circular disposition, indicating that these two modes represent a cyclic phenomenon of a single frequency.

4.2.2 Linear coefficients of dynamical system

The scalar products $(\Phi_{,x}^{(i)}(\mathbf{x}), \Phi^{(j)}(\mathbf{x}))$ are presented in figure 19. As predicted by equation 15, we can see that the scalar products are close to zero for $i = j$ meaning that the POD modes are orthogonal to their derivatives. This is again a clear sign that the POD analysis mostly captures the advective motion of the flow.

The equation 18 states that, in the case of an advective

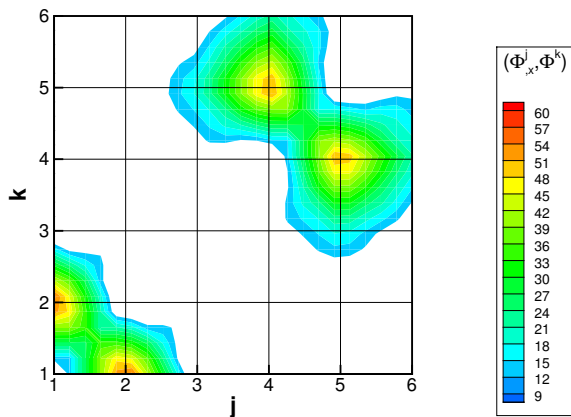


Fig. 19 Scalar products values $(\Phi_{,x}^{(i)}(\mathbf{x}), \Phi^{(k)}(\mathbf{x}))$. Note that values out of a grid point are interpolated.

tive motion, the coefficient of a linear dynamical system of POD modes can be obtained using the scalar product of the spatial POD modes and their spatial derivatives. Since these coefficients can be related to the frequency of this simple dynamics (see equation 24), it is possible to compute the expected values of the scalar products $(\Phi_{,x}^{(i)}(\mathbf{x}), \Phi^{(j)}(\mathbf{x}))$. Main flow features oscillate at a known pulsation $\omega = 2\pi f_s$ (see figures 8 and 13) and the convective velocity U_c is also known (see figure 15), we would expect that $(\Phi_{,x}^{(1)}(\mathbf{x}), \Phi^{(2)}(\mathbf{x})) = \omega/U_c \simeq 80m^{-1}$. From figure 19, the largest values of the scalar product are obtained for $(\Phi_{,x}^{(1)}(\mathbf{x}), \Phi^{(2)}(\mathbf{x}))$ and $(\Phi_{,x}^{(2)}(\mathbf{x}), \Phi^{(1)}(\mathbf{x}))$. However, the maximum value is of about $60m^{-1}$ which is lower than expected. This may rise for different reasons: either the convective speed of the structures capture by the POD is not equal to the one measured with the schlieren images, or the computation of the spatial derivatives amplified the noise contained in the modes and the POD modes do not perfectly project onto their spatial derivatives. The latter is most probable, the PIV data contains only 200 samples which may not be sufficient to converge the POD analysis to an acceptable uncertainty.

The linear dynamical system identified is presented in the figure 20. The initial condition was chosen so that the overall dynamics is representative of the entire data and the model was run using a fourth order Runge-Kutta algorithm. We clearly see that the derived dynamical system well passes in the average circle described by the measurement points. However, it is clear that a simple linear dynamics does not suffice to represent well the more complicated dynamics extracted with the POD modes. This shows that the POD modes extracted do not only represent a convective motion, and thus the POD-advection model can only represent a portion of the original dynamics.

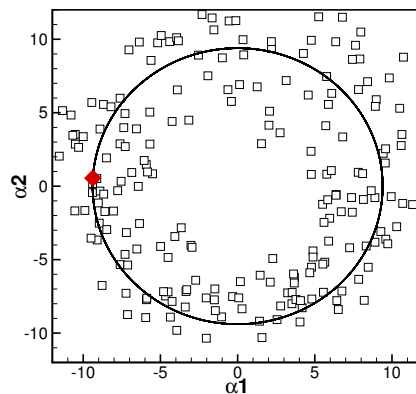


Fig. 20 Phase portrait of temporal POD modes $\alpha^{(2)}(t)$ as a function of $(\alpha^{(1)}(t))$. The line is the linear dynamical system identified with the method presented in paragraph 2. The red dot is the initial condition of the dynamical system.

5 Conclusion

The POD is a widely used technique that was originally designed in order to educe the most energetic structures in the flow. Applying the POD to the advection equation results in a system of equations that links the temporal and spatial POD modes, and their respective derivative to the convection speed of the flow.

We have shown in this paper that these results can be used to estimate the convection velocity of coherent features. For this purpose, the data does not have to be time-resolved nor need to originate from a complicated measurement campaign. Indeed, dual-time information obtained with Schlieren images can suffice to obtain estimate of the convection velocity.

An original feature of the model developed in this paper is that it allows for the construction of a linear dynamical system even if the original data is only made of independent realizations. The only *a priori* knowledge

of a convection speed allows to reproduce and simulate the main dynamics of eligible flow fields, *i.e.* flows governed by convective motion where a simple dynamics seems to dominate. This can help in order to understand at least part of the dynamics, as was the case here, of complicated flows, especially if time-resolved data cannot be obtained.

The present paper focuses on presenting the methodology and how it can be used with experimental data. However, since purely experimental data were used in this study, any conclusions regarding the uncertainty and bias of the proposed method is a combined effect of both the measurement uncertainties and the method itself. Although the results showed in this paper are encouraging, some more analysis, beyond the scope of this paper, would be required to reduce the sensitivity of the method with respect to experimental parameters.

acknowledgments

The authors wish to thank the Region Poitou-Charentes and DGA-Spae for supporting part of this study.

References

- Adrian RJ (1991) Particle imaging techniques for experimental fluid mechanics. *Annu Rev Fluid Mech* 23:261–304
- Alkisar MB, Krothapalli A, Lourenco LM (2003) Structure of a screeching rectangular jet : a stereoscopic particle image velocimetry study. *Journal of Fluid Mechanics* 489:121–154
- Berland J, Bogey C, Baily C (2007) Numerical study of screech generation in a planar supersonic jet. *Physics of fluids* 19
- Delville J (1995) La décomposition orthogonale aux valeurs propres et l'analyse de l'organisation tridimensionnelle des écoulements turbulents cisailés libres. PhD thesis, Université de Poitiers, France
- Edgington-Mitchell D, Oberleithner K, Honnery DR, Soria J (2014) Coherent structure and sound production in the helical mode of a screeching axisymmetric jet. *Journal of Fluid Mechanics* 748:822–847
- Jaunet V (2010) Etude d'un jet rectangulaire supersonique à nombre de mach 1.45 vectorisé par actionneur fluide. PhD thesis, Université de Poitiers, FRANCE
- Jaunet V, Aymer D, Collin E, Bonnet JP, Lebedev A, Fourment C (2010) 3d effects in a supersonic rectangular jet vectored by flow separation control, a numerical and experimental study. *AIAA paper* 2010-4976
- Kerherve F, Jordan P, Gervais Y, Valière JC, Braud P (2004) Two-point laser doppler velocimetry measurements in a mach 1.2 cold supersonic jet for statistical aeroacoustic source model. *Experiments in Fluids* 37(3):419–437, DOI 10.1007/s00348-004-0815-1, URL <http://dx.doi.org/10.1007/s00348-004-0815-1>
- Lammari MR (1996) Mesures par vélocimétrie laser doppler dans une couche de mélange turbulente supersonique : quelques aspects du processus de mesure. PhD thesis
- Lumley JL (1967) The structure of inhomogeneous turbulent flows. *Atm Turb and Radio Wave Prop* pp 166–178
- Morris PJ, Zaman K (2010) Velocity measurements in jets with application to noise source modeling. *Journal of Sound and Vibration* 329(4):394 – 414
- Murray N, Ukeiley L (2007) An application of gappy pod. *Experiments in Fluids* 42(1):79–91, DOI 10.1007/s00348-006-0221-y, URL <http://dx.doi.org/10.1007/s00348-006-0221-y>
- Papamoschou D (1989) A two-spark schlieren system for very-high velocity measurement. *Exp In Fluids* 7:354–356
- Perret L, Collin E, Delville J (2006) Polynomial identification of POD based low-order dynamical system. *Journal of turbulence* 7
- Powell A (1953a) On the mechanism of choked jet noise. *Proceedings of the Physical Society of London* B66:1039–1056
- Powell A (1953b) On the noise emanating from a two dimensional jet above the critical pressure. *Aeronautical quarterly* 4:103–122
- Raman G (1999) Supersonic jet screech : half-century from powell to the present. *J of Sound and Vib* 225:543–571
- Scarano F (2002) Iterative image deformation methods in piv. *Meas Sci Tech* 13:R1–R19
- Shih C, Lourenco L, Krothapalli A (1995) Investigation of flow at leading and trailing edges of pitching-up airfoil. *AIAA Journal* 33(8):1369–1376
- Sirovich L (1987) Turbulence and the dynamics of coherent structures. part 1 : coherent structures. *Quarterly of applied mathematics* XLV
- Soria J (1996) An investigation of the near wake of a circular cylinder using a video-based digital cross-correlation particle image velocimetry technique. *Experimental Thermal and Fluid Science* 12:221–233
- Westerweel J, Scarano F (2005) Universal outlier detection for piv data. *Experiments in Fluids* 39(6):1096–1100, DOI 10.1007/s00348-005-0016-6, URL <http://dx.doi.org/10.1007/s00348-005-0016-6>

Willert CE, Gharib M (1991) Digital particle image velocimetry. *Experiment in FLuids* 10:181–193